Nanoscale Advances

ROYAL SOCIETY OF CHEMISTRY

PAPER

View Article Online
View Journal | View Issue

Cite this: *Nanoscale Adv.*, 2023, **5**, 2226

Kilogram-scale fabrication of TiO_2 nanoparticles modified with carbon dots with enhanced visible-light photocatalytic activity†

Jingjing Xu, ‡[a] Jiayan Zhang, ‡[a] Feifei Tao, *[ab] Pengfei Liang [a] and Pingan Zhang [a]

Incorrect discharge of dye wastewater will cause environment pollution and be very harmful to human health. Visible-light photocatalysis over large-scale synthesized semiconductor materials can become one of the feasible solutions for the practical application of purifying dye wastewater. As a new candidate, carbon dots (CDs) with unique fluorescence were fabricated on a tens of grams scale and then further applied to the kilogram-scale synthesis of a CDs/TiO_2 composite by one-step heat treatment. Compared with single TiO_2 nanoparticles (NPs), the CDs/TiO_2 composite with a large specific surface area exhibits enhanced photo-degradation performance for methyl orange (MO). This phenomenon can be attributed to the loading of CDs in the TiO_2 NPs, which is conducive to broadening the light absorption spectrum and improving absorption intensity, narrowing the band gap, charge carrier trapping, up-converting properties, and charge separation. The kilogram-scale synthesis of the CDs/TiO_2 photocatalyst does not affect the morphology, structure, optical properties and photocatalytic performance of the composite, which opens up a new avenue to construct elaborate heterostructures for enhanced photocatalytic performance using visible light as the light source.

Received 3rd December 2022
Accepted 27th February 2023

DOI: 10.1039/d2na00886f

rsc.li/nanoscale-advances

1. Introduction

In the face of rapid industrial growth, the crisis caused by energy shortage and environmental deterioration has become one of the most critical issues and has threatened the sustainable development of mankind in recent years.[1,2] The alarming discharge of organic dye contaminants from the textile industry has brought about serious water pollution, which affects the natural environment and seriously harms human health.[3–5] In order to solve these problems, various technologies, such as physical adsorption,[6] membrane filtration,[7] biodegradation,[8] Fenton processes,[9] electrochemical methods[10] and photocatalytic degradation,[11] are applied to get rid of organic dye pollutants in wastewater. Among them, visible-light photocatalysis over semiconductors is an economic, efficient and sustainable method, because it can make the best of renewable and clean solar energy to remove organic pollutants in wastewater.[12,13] Although many achievements have been made in visible-light photocatalysis, the practical application of large-scale photocatalytic materials with excellent activity and stability is still not realized, which involves complex and expensive synthesis. Therefore, it is urgently needed to develop scalable and facile synthesis of photocatalysts with efficient visible-light utilization and long-term stability.

The facile synthesis of photocatalytic materials is crucial to obtain excellent photocatalytic performance.[14] Nowadays, many semiconductors with micro- and nano-structures have been prepared to act as photocatalysts, including TiO_2,[15] ZnO,[16] Fe_2O_3,[17] SnO_2,[18] Co_3O_4,[19] and so on. Among them, TiO_2 is considered as the most widely studied semiconductor with many characteristics including low cost, non-toxicity, excellent photocatalytic properties and stability.[20,21] However, TiO_2 also has some shortcomings of a large band gap (~3.2 eV) and the fast recombination of photo-excited charge carriers. These seriously restrict the use of solar energy and the improvement of photocatalytic properties.[22] To solve the above problems, a large number of solutions have been reported including controlling morphologies,[23,24] doping[25] and constructing semiconductor composites.[26] Among them, the modification of carbonaceous materials in TiO_2 may be a feasible method to obtain visible-light photocatalysts.

Carbon dots (CDs) as a new type of fluorescent carbon nanomaterial have the characteristics of non-toxicity, low cost, a wide source of raw materials and good biocompatibility.[27] Therefore, CDs display broad application prospects in many

[a]*Department of Chemistry and Chemical Engineering, Shaoxing University, Zhejiang 312000, P. R. China. E-mail: feifeitao@usx.edu.cn*

[b]*Shanghai Advanced Research Institute, Chinese Academy of Sciences, Shanghai 201210, P. R. China*

† Electronic supplementary information (ESI) available. See DOI: https://doi.org/10.1039/d2na00886f

‡ These authors contributed equally to this paper and should be considered as co-first authors.

fields, such as biology,[28] optoelectronics[29] and photocatalysis.[30] CDs not only have the fluorescence characteristics of traditional quantum dots, such as emitting fluorescent light, controlling excitation and emission wavelengths and up-conversion luminescence, but also serve as electron donors and acceptors.[31,32] Coupling CDs with other semiconductors can be used to broaden the absorption spectrum, promote the charge separation and transfer, and enhance the photocatalytic activity.[33–35] However, the low-cost and efficient preparation of CDs is scarce, which limits the large-scale synthesis of CD-based photocatalysts and practical application in photocatalysis. Therefore, it is urgent to explore a feasible large-scale route to design a CDs/TiO_2 composite with a broadened light response range and enhanced photocatalytic properties.

In this paper, glucose was used for the large-scale preparation of CDs, and the kilogram-scale synthesis of CDs/TiO_2 composites was realized by a simple heat treatment method. Due to the unique up-conversion of CDs, the interfacial interaction and the narrowed band gap, the kilogram-scale CDs/TiO_2 composites exhibit superior photocatalytic properties when irradiated with visible light and excellent stability for the degradation of methyl orange (MO).

2. Experimental

2.1 Synthesis

2.1.1 Preparation of TiO_2 nanoparticles (NPs). Tetrabutyl titanate (4 mL) was added to absolute ethanol (50 mL) with intense stirring, followed by the addition of deionized water (1 mL). The obtained mixture was centrifuged and washed repeatedly with deionized water. After being dried at 60 °C overnight, the product was taken out and ground to obtain TiO_2 NPs. The gram-scale TiO_2 NPs were synthesized by magnifying the raw materials by 50 times based on the above the preparation.

2.1.2 Preparation of carbon dots (CDs). Glucose (1.80 g) and sodium hydroxide (NaOH, 0.16 g) were dissolved successively in deionized water (10 mL) with stirring. After NaOH was completely dissolved, the solution was neutralized with hydrochloric acid to pH = 7. After being dried at 80 °C for 12 h, the powder was transferred to a muffle furnace at 300 °C for 1 h. The fluffy black solid obtained was washed with ethanol and deionized water in turn, dried and ground to obtain CDs. The gram-scale preparation of CDs (gCDs) can be achieved by magnifying the raw materials by 50 times based on the ratio of original materials.

2.1.3 Preparation of the CDs/TiO_2 composites. A certain amount of TiO_2 NPs and CD powder was ground for at least 10 min and then heated in a muffle furnace at 300 °C for 1 h. When the content of CDs in the mixture is 0.5, 1.0, 2.0, 3.0 and 4.0 wt%, the obtained CDs/TiO_2 composites are denoted as CT0.5, CT1, CT2, CT3 and CT4, respectively.

2.1.4 Preparation of the kilogram-scale CDs/TiO_2 composites (kCT2). The obtained gram-scale CDs (gCDs) and TiO_2 NPs were used as raw materials. When the content of gCDs in the mixture is 2.0 wt%, the obtained CDs/TiO_2 composite is denoted as kCT2 using the same preparation method as the CDs/TiO_2 composite.

2.2 Characterization

The morphologies, structures and lattice fringes were detected by using a scanning electron microscope (SEM, JSM-6360 LV) and high resolution transmission electron microscope (HRTEM, JEM-2100F). The chemical composition was detected *via* energy dispersive X-ray spectroscopy (EDS) analysis and elemental mapping. The crystal structure was characterized by powder X-ray diffraction (XRD, Empyrean XRD-6000, Cu Kα radiation, and λ = 0.15406 nm). The functional groups were measured by Fourier transform infrared spectroscopy (FT-IR, VERTEX70) and Raman spectroscopy on a Horiba LabRAM HR Evolution with a 632.8 nm laser. N_2 adsorption–desorption isotherms were obtained on a TriStar 3020. X-ray photoelectron spectra (XPS) were collected on a Physical Electronics PHI 1600 ESCA system (monochromatic Al Kα source, 1486.6 eV). Ultraviolet visible (UV-vis) spectra and photoluminescence (PL) curves were recorded on a UV-2550 and F-7000, respectively. Time-resolved photoluminescence (TRPL) spectra were recorded on a FluoTime 300 (picoQuant GmbH) using a laser of 405 nm. The surface photovoltage (SPV) spectra were obtained on a home-built apparatus including a source for monochromatic light, a double-grating monochromator (Zolix SP500), a lock-in amplifier (SR830-DSP) and an optical chopper (SR540) at a testing frequency of 24 Hz.

2.3 Photoelectrochemical measurements

The photoelectrochemical performance was characterized on an electrochemical analyser (CHI 760E, Shanghai Chenhua, China) with a 300 W xenon lamp (λ > 420 nm). An Ag/AgCl electrode (saturated KCl) and platinum foil were used as the reference electrode and counter electrode, and 0.5 M Na_2SO_4 aqueous solution as the electrolyte solution. After ultrasonic cleaning with acetone and deionized water in turn, the F-doped tin oxide (FTO) glass was placed under an infrared lamp to dry. The catalyst was put in absolute ethanol to make the slurry (1.0 g L^{-1}) by sonication for at least 30 min. 0.1 mL of the above slurry was coated on the conductive surface of the cleaned FTO glass. After natural drying in air, the modified FTO glass was treated at 300 °C for 1 h to construct the working electrode with an active area of 0.196 cm^2.

2.4 Photocatalytic degradation

The photocatalyst (30 mg) was added to the MO aqueous solution (30 mL and 10 mg L^{-1}) under the action of ultrasound. After stirring in the dark for at least 30 min, the suspension was irradiated with a 300 W xenon lamp (λ > 420 nm). A certain amount of the reaction mixture was sampled every once in a while and centrifuged. The supernatant was measured at the maximum absorption of MO on a UV-vis spectrometer (UV-2550) to evaluate the MO removal. The stability was determined in 5 cycles of photocatalytic tests. After each photocatalytic reaction, the sample was washed with plenty of deionized water and dried at 60 °C for the next cycle.

2.5 Active species trapping experiments

To determine the active species, *tert*-butyl alcohol (TBA), benzoquinone (BQ) and disodium ethylenediaminetetraacetate

dehydrate (EDTA-2Na) at the same concentration of 1.0 mmol L^{-1} were used as a scavenger to detect hydroxyl radicals ($\cdot OH$), superoxide radicals ($\cdot O_2^-$) and photo-generated holes (h^+), respectively. The experiment was similar to the MO photocatalytic test.

To detect the $\cdot O_2^-$ amount during the photocatalytic process, 20 mg of photocatalyst was added to 50 mL of nitroblue tetrazolium (NBT) solution (2.5×10^{-5} mol L^{-1}) under ultrasonication. The concentration of NBT was evaluated by recording the maximum absorption peak of NBT at 259 nm on a UV-2550 UV-vis spectrophotometer.[36] The generated $\cdot OH$ radicals were determined by using a terephthalic acid (TA) probe molecule on a Fluoromax-3 spectrometer. In detail, the photocatalyst (20 mg) was added to TA solution (50 mL, 5×10^{-4} mol L^{-1} in 2×10^{-3} mol L^{-1} NaOH). The 2-hydroxyterephthalic acid (2-TAOH) from the reaction of TA and $\cdot OH$ has a characteristic fluorescence emission of about 425 nm at the 300 nm excitation wavelength.[36]

3. Results and discussion

3.1 Structure, composition and morphology

The TiO_2 NPs and the CDs/TiO_2 composites were investigated by using XRD patterns in Fig. 1a. For TiO_2 NPs, the diffraction peaks at 25.4°, 37.8°, 48.1°, 54.0°, 55.2°, 62.4°, 69.3° and 75.5° coincide well with the (101), (004), (200), (105), (211), (204), (116) and (215) crystal planes of typical anatase TiO_2 (JCPDS card no. 21-1272).[37] All the CDs/TiO_2 composites including kCT2 display the XRD curves similar to TiO_2 NPs, implying no effect of the modification of CDs on the original crystal structure of TiO_2 NPs. The diffraction peaks assigned to CDs couldn't be found in the XRD curves of all the composites, which may be ascribed to the amorphous features and/or the low content of CDs.

The SEM and HRTEM images in Fig. S1† and 1b are used to explore the morphologies of TiO_2 NPs, CDs and the CDs/TiO_2 sample. The as-prepared TiO_2 sample has a sphere-like structure with a uniform size of 200–400 nm (Fig. S1a†). According to the further HRTEM observation (Fig. S1b†), the spherical morphology is composed of a large number of nanoparticles of about 5–10 nm. These nanoparticles agglomerate with each other, leading to low dispersion. In Fig. S1c,† there are a large number of obvious lattice fringes of $d = 0.352$ nm that belong to the (101) crystal plane of anatase TiO_2.[38,39] The HRTEM image shows that the CDs with a diameter of 2–5 nm are well monodispersed and have a nearly spherical shape (Fig. S1d†). At the same time, the absence of lattice fringes indicates the poor crystallinity of the CDs. It is observed from the SEM image (Fig. 1b) that CT2 has a similar sphere-like morphology and size to TiO_2 NPs, suggesting that the modification of CDs doesn't destroy the original shape of TiO_2 NPs. And the CT2 sample is also composed of a large number of TiO_2 NPs and CDs (Fig. 1c and d). The introduction of CDs into TiO_2 NPs can help to inhibit the agglomeration of TiO_2 NPs. According to the obvious lattice fringes ($d = 0.352$ nm) attributed to the (101) crystal plane of TiO_2,[38,39] it is proved that TiO_2 NPs and CDs are intertwined with each other, implying the existence of interaction at their interface.[40] Meanwhile, Fig. S2† shows the SEM and HRTEM images of kCT2, which has a similar morphology to CT2. The optical photo of kCT2 indicates the kilogram-scale synthesis of CT2, confirming that the method can realize the kilogram-scale preparation of the photocatalyst. Combined with the XRD result, it is found that the amplification of the synthesis reaction doesn't destroy the shape and crystal structure of the products. This facile method to obtain the CDs/TiO_2 composite on a large scale provides a promising path for massive applications of photocatalysts.

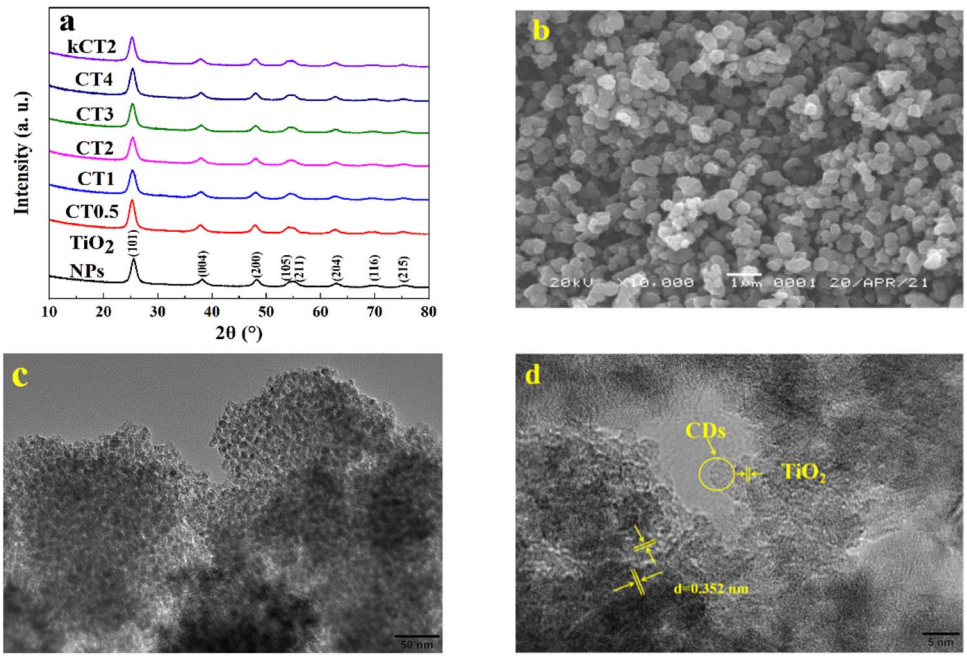

Fig. 1 XRD patterns of TiO_2 NPs and CDs/TiO_2 (a), SEM (b), and HRTEM images (c and d) of CT2.

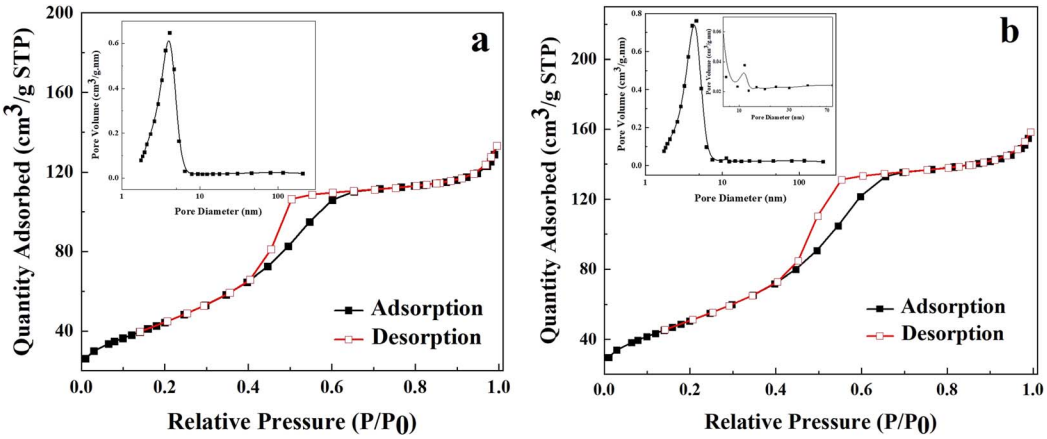

Fig. 2 N_2 adsorption–desorption curves and pore size distribution (inset) of TiO_2 NPs (a) and kCT2 (b).

The CDs/TiO_2 composite synthesized on the kilogram scale (kCT2) was further investigated by EDS and elemental mapping (Fig. S3†). The EDS result confirms that the kCT2 consists of Ti, O and C elements, and the carbon content is 1.98 wt%. This value is very consistent with the addition amount of CDs of 2.0 wt% in the preparation process, suggesting that there is almost no less of CDs in the synthesis of kCT2. It is further confirmed by the elemental mapping diagrams that all elements are evenly distributed and CDs are uniformly dispersed in the TiO_2 NPs, just like CT2 (Fig. 1c and d). Compared with Ti and O elements, the sparser distribution of C element proves the low content of CDs in kCT2 from the EDS result, which explains the absence of the XRD diffraction peak of CDs in the composites combined with weak crystallinity.

The HRTEM image clearly displays the porous features of the composite, which can be investigated by the BET measurement, as depicted in Fig. 2. The N_2 adsorption–desorption curves of TiO_2 NPs and kCT2 can be attributed to type IV isotherms with a H2 hysteresis loop in the relative pressure (P/P_0) range of 0.4–0.7, implying mesoporous properties.[41,42] The specific surface areas of TiO_2 NPs and kCT2 are 162.85 and 185.78 $m^2\ g^{-1}$, respectively. The higher specific surface area of kCT2 may be ascribed to the specific hierarchical structure and the modification of TiO_2 NPs by CDs with a small size, which can effectively alleviate the aggregation of nanoparticles.[43] It can be further observed in the insets of Fig. 2 that the pore size of TiO_2 NPs and kCT2 is mainly concentrated at about 4.1 and 4.6 nm by the BJH method from the gas escape during the heat treatment. In addition, from the enlarged pore size distribution of kCT2, there is another type of pore at about 11 nm, possibly due to the loading of CDs. The modification of TiO_2 NPs with CDs leads to a larger specific surface area and more pores, which generally favour adsorption and photocatalysis.[44]

The surface functional groups of TiO_2 NPs and CDs/TiO_2 were further evaluated by FT-IR and Raman analyses (Fig. 3). For TiO_2 NPs, the broad absorption at 450–750 cm^{-1} is assigned to the bending and stretching vibrations of the Ti–O–Ti bond.[45–47] The absorption peaks at 1632 and 3450 cm^{-1} correspond to the bending vibration of the O–H group and the stretching vibration of hydrogen-bonded water molecules and adsorbed hydroxyl groups on the surface.[48] The CDs/TiO_2 composites display similar FT-IR curves and absorption bands to TiO_2 NPs, suggesting that the addition of CDs in the samples causes no obvious damage to the surface functional groups of TiO_2 NPs.

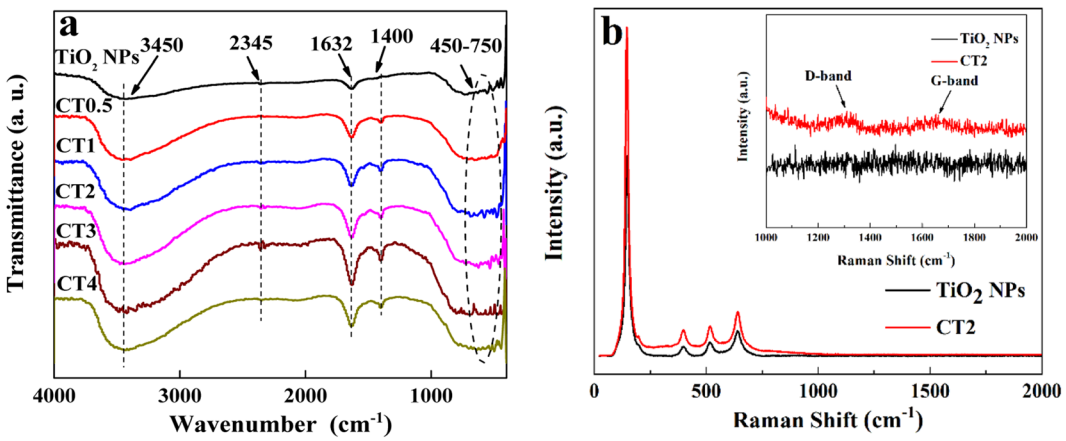

Fig. 3 FT-IR spectra of TiO_2 NPs and CDs/TiO_2 (a), and Raman spectra of TiO_2 NPs and CT2 (b).

The peaks at 2345 and 1400 cm^{-1} belonging to the stretching vibration of C=C (ref. 49) and C–O (ref. 37 and 50) can be found only in the composites and become stronger and slightly blue shift with the increase of the CD content, due to the existence of interaction between CDs and TiO_2 NPs.[50] In Fig. S4†, kCT2 shows a similar FT-IR spectrum to the CDs/TiO_2 composites, suggesting that the CDs are successfully modified in TiO_2 NPs and the amplification of the reaction has no effect on the surface functional groups of the composite. In addition, the effect of the modification of CDs on the surface composition and structures of TiO_2 NPs was further investigated by Raman spectroscopy (Fig. 3b). TiO_2 NPs clearly exhibit four characteristic bands at about 145, 399, 518 and 643 cm^{-1} corresponding to the anatase phase of TiO_2.[37,51] For CT2, the introduction of CDs into TiO_2 NPs causes a slight blue shift of the peaks at about 518 and 643 cm^{-1}, further confirming the existence of the interface interaction.[40] Moreover, in addition to the anatase peaks of TiO_2, there are two weak characteristic bands in CT2 corresponding to 1312 cm^{-1} (D-band) and 1620 cm^{-1} (G-band). The D-band is related to the vibration of carbon atoms with dangling bonds in the plane terminations of disordered graphite, and the G-band is indexed to the in-plane vibration of sp^2 hybridized carbon atoms.[37,40,52] Therefore, these results provide the evidence of existence of CDs in the composite.

XPS measurement was conducted to further examine the chemical composition and bonding configuration of the

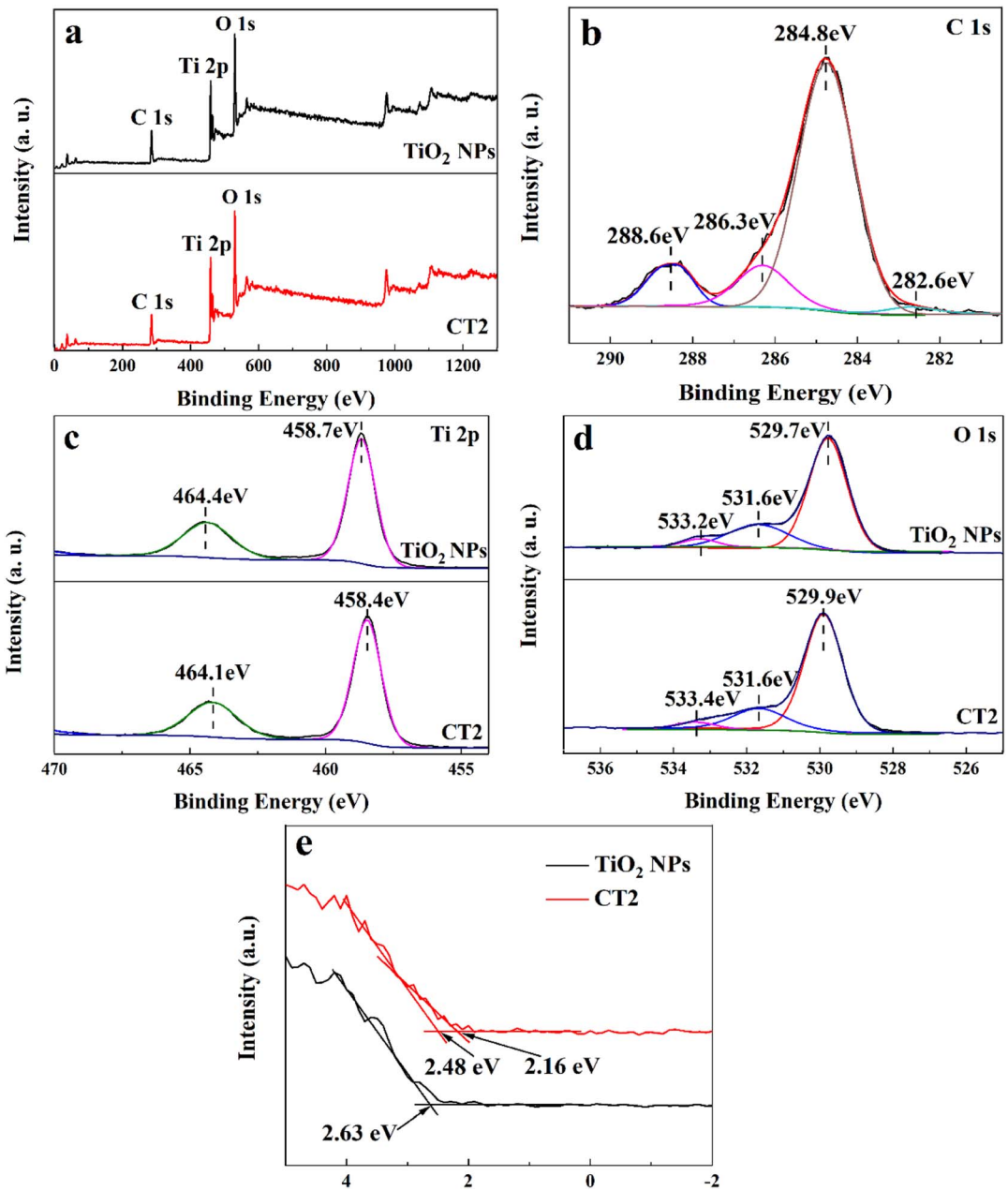

Fig. 4 XPS survey spectra (a), the corresponding high-resolution XPS spectra (b–d) of C 1s (b), Ti 2p (c) and O 1s (d), and VB-XPS spectra (e) of TiO_2 NPs and CT2.

photocatalyst. Based on the XPS survey spectra (Fig. 4a), both TiO_2 NPs and CT2 contain Ti and O, and C element appears in CT2. The C element detected in TiO_2 NPs might be due to adventitious hydrocarbon in the XPS instrument. According to the deconvolution spectrum of C 1s in Fig. 4b, CT2 displays four peaks at 282.6, 284.8, 286.3 and 288.6 eV, indicating different types of C states. The deconvoluted C 1s peak at 284.8 eV is assigned to C–C bonds in adventitious carbon and sp^2-hybridized carbon from aromatic networks.[53–55] The other C 1s peaks at 286.3 and 288.6 eV represent the oxygen bound species C–O and C=O,[55,56] which provides the evidence that the carbon is incorporated into the lattice of TiO_2 by substitution in the lattice of titanium sites or interstitial sites[55,57] and oxidized to carbonate species during the heating treatment.[54,55] And when the TiO_2 NPs are modified with CDs, the C 1s peak at 282.6 eV is detected, indicating that the oxygen may be substituted in the lattice of TiO_2 as the Ti–C bond.[57–59] This strongly suggests the existence of the carbon in TiO_2 from the binding energies of the electrons.[58] In Fig. 4c, the Ti 2p peaks of TiO_2 NPs at 458.7 and 464.4 eV are assigned to Ti $2p_{3/2}$ and Ti $2p_{1/2}$,[56,60] due to spin-orbital doublet splitting, suggesting an oxidation state of Ti^{4+}. And the slight red shift of Ti 2p peaks in CT2 suggests the coupling of TiO_2 and carbon.[59] For the O 1s spectrum of TiO_2 NPs, the peaks at 529.7 and 531.6 eV belong to lattice oxygen (Ti–O) and absorbed oxygen (O–H), respectively.[61] The higher peak at 533.4eV can be defined as the C–O bond,[53,61] further confirming the existence of the CDs. Compared to TiO_2 NPs, the location of oxygen element in CT2 is shifted slightly toward higher binding energy, which may be due to the increase of charge density from the substitution of titanium in the TiO_2 lattice of CT2 by carbon atoms.[55] The above results reveal that the CDs/TiO_2 composite is composed of TiO_2 and CDs, not their mechanical mixture, and contains various carbon species such as lattice carbons and substitutional and interstitial carbons, and the amplified synthesis has little effect on the chemical composition and bonding configuration of the composite.

The electronic structures of TiO_2 NPs and CT2 were further evaluated by VB-XPS (Fig. 4e). The binding energy of CT2 is smaller than that of TiO_2 NPs and valence band (VB) tail states are observed only in CT2. This band tail phenomenon may be due to the strong electron withdrawing ability of the carboxylate groups, thereby causing additional diffusive electronic states above the VB edge and a narrowed band gap.[55,62,63]

3.2 Photocatalytic activity

The photocatalytic degradation of the MO solution was carried out over the CDs/TiO_2 composites with a 300 W xenon lamp ($\lambda >$ 420 nm). In control experiments (Fig. 5a), about 9.0% of MO over CT2 is removed without light. At an irradiation time of 120 min, the removal of MO is only 6.5% in the absence of the photocatalyst. The results of the above control experiments show that both the photocatalyst and illumination are essential for the removal of MO. When bare TiO_2 NPs are used as the photocatalyst, about 12.4% of MO is removed under irradiation for 120 min. However, when CDs are loaded in TiO_2 NPs, the removal efficiency of MO is surprisingly improved. And when the content of CDs increases, the removal of MO first goes up and then down. This may be attributed to the fact that the excess CDs in the composite could obstruct the reaction active sites or become a recombination centre, and instead inhibit the separation of charges.[64] And the CT2 sample can remove 88.8% of MO, exhibiting the highest photocatalytic activity under irradiation of 120 min. Under the same photocatalytic conditions, 88.6% of MO over kCT2 can be removed, suggesting that the kilogram-scale synthesis of the composite will not reduce its

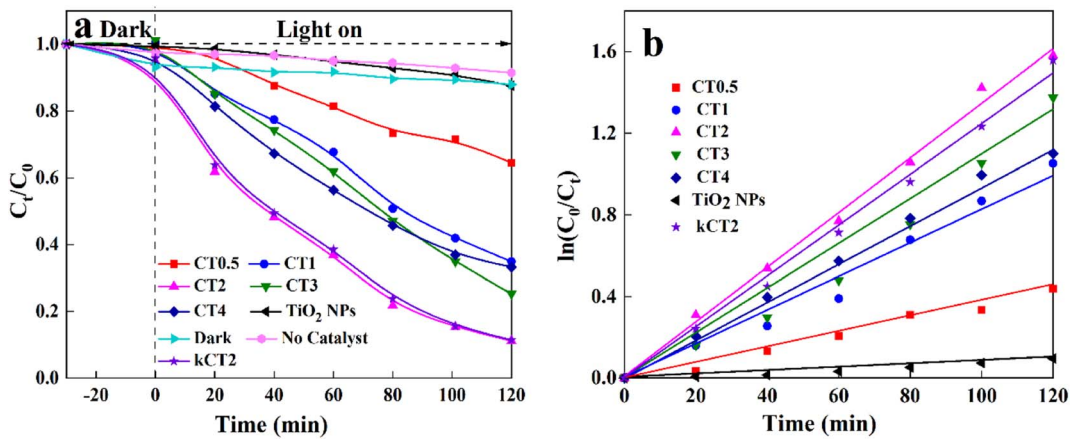

Fig. 5 Photocatalytic activities of MO (a) and kinetic linear simulation for various photocatalysts (b).

Table 1 K_{app} of MO degradation over various photocatalysts

Photocatalyst	TiO_2 NPs	CT0.5	CT1	CT2	CT3	CT4	kCT2
K_{app} (min^{-1})	0.0009	0.0034	0.0065	0.0128	0.0096	0.0080	0.0127

catalytic activity. The above results indicate that the CDs/TiO_2 composites can greatly degrade the MO solution irradiated with visible light, and the corresponding kinetics simulation was investigated as shown in Fig. 5b in a pseudo first-order Langmuir–Hinshelwood (L–H) mode.[65,66] Apparently, the apparent first-order rate constant (K_{app}) of the CDs/TiO_2 composites obviously exceeds that of TiO_2 NPs (Table 1). Moreover, the CT2 displays the largest K_{app} of 0.0128 min^{-1}, which is similar to that of kCT2 and 14.2 times that of TiO_2 NPs.

In comparison to the as-obtained CDs/TiO_2 composite, the photocatalytic performance of MO over the non-metallic coupled TiO_2 photocatalysts is shown (Table S1†). Various non-metallic coupled TiO_2 composites can promote the MO degradation under their own catalytic conditions. By comparison, the as-obtained CDs/TiO_2 composites can exhibit satisfactory removal of MO, indicating their potential application in wastewater treatment.

The photocatalytic stability test of the CDs/TiO_2 sample is performed as shown in Fig. 6. After five consecutive runs, the MO solution can still be effectively removed over CT2 and kCT2. The photocatalytic removal of MO after five cycles still remains at 84.9% for CT2 and 84.7% for kCT2, close to 88.8 and 88.6% of the first removal rate of MO. The used kCT2 after five cycles still displays a crystal structure and morphology similar to the unreacted one (Fig. S6†). Therefore, the CDs/TiO_2 composites can act as a good and stable photocatalyst and exhibit potential to alleviate the pollution of industrial wastewater.

3.3 Photocatalytic mechanism

The kCT2 sample has a similar morphology, crystallinity, surface structure, chemical composition and photocatalytic performance to CT2, so kCT2 is used to make clear the photocatalytic mechanism of the MO degradation. Both the light absorption capacity and the charge separation are the key indicators for evaluating the photocatalytic performance.

The light absorbance properties are usually characterized by UV-vis spectroscopy. TiO_2 NPs exhibit the absorption of ultraviolet light in accordance with the intrinsic absorption properties of TiO_2 (Fig. 7a).[67] The CDs display significant absorption in the ultraviolet light region and the visible light region. When the CDs are introduced into TiO_2 NPs, the CDs/TiO_2 composites show UV-vis spectra similar to those of TiO_2 NPs and CDs, but their light absorption intensity and range significantly exceed those of TiO_2 NPs and CDs. Therefore, the existence of CDs can improve the visible-light photocatalysis of TiO_2 NPs. Moreover, when the content of CDs increases, the absorption peak shows the intensity change of first increasing and then decreasing, and kCT2 displays the strongest light adsorption capability. This may be because TiO_2 NPs are covered by too many CDs, leading to the formation of photoelectron recombination centers.[68] Based on the calculation of the Kubelka–Munk formula from the Tauc plot,[69] the band gap is measured to be 3.21 eV for TiO_2 NPs and 3.10 eV for kCT2 (Fig. 7a inset). The introduction of CDs into TiO_2 NPs decreases the band gap energy and enhances the visible-light absorption,[70] possibly due to the existence of the interaction between TiO_2 NPs and CDs,[71] so as to promote visible-light photocatalysis.

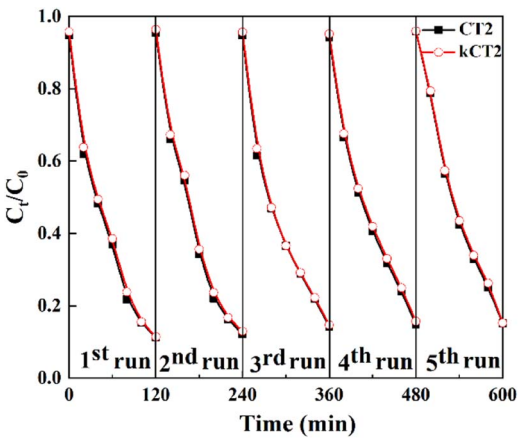

Fig. 6 Five consecutive cycles of photocatalytic degradation of MO over CT2 and kCT2.

The photoluminescence (PL) emission spectrum of the photocatalyst can be used to characterize the charge separation efficiency, and a lower PL intensity means a longer lifetime of charges.[67,70] In Fig. 7b, the TiO_2 NPs have a strong and broad PL response at about 425 nm, while the CDs/TiO_2 composites display a very weak PL peak and kCT2 has the lowest PL intensity. This means that the CDs/TiO_2 composites, especially kCT2, might have a long life of charges.[70] This was further explored by time-resolved photoluminescence (TRPL) spectroscopy that can be applied to evaluate the electron transfer dynamics based on the emission lifetime (Fig. 7c).[72,73] Generally speaking, a longer emission lifetime means a lower recombination of charges. Both TiO_2 NPs and kCT2 exhibit an exponential decay fitted *via* bi-exponential function formula (1):

$$I(t) = A_1 e^{\frac{-t}{\tau_1}} + A_2 e^{\frac{-t}{\tau_2}} \quad (1)$$

where A_i is the amplitude and τ_i is the lifetime. The lifetime is contributed by the non-radiative process (τ_1) and the radiative process (τ_2). And τ_2 is directly relevant to the separation of photo-excited electrons and holes. Moreover, the average lifetime τ_{ave} is calculated by formula (2):

$$\tau_{ave} = \frac{A_1\tau_1^2 + A_2\tau_2^2}{A_1\tau_1 + A_2\tau_2} \quad (2)$$

And the fitted lifetimes are listed in Table 2. The kCT2 sample shows a τ_{ave} value (3.03 ns) higher than that of TiO_2 NPs (2.35 ns) and its longer lifetime indicates that the charge recombination is inhibited.[72]

Up-conversion luminescence is considered a short wavelength emission by absorbing long wavelength light.[5] The emission spectra of the gCDs were clearly detected under the excitation light of 400–850 nm (Fig. 7d). The emission of the gCDs becomes stronger with the increasing excitation of 400–750 nm and then weakens with excitation from 750 to 850 nm. It is surprisingly observed that the broad emission in the

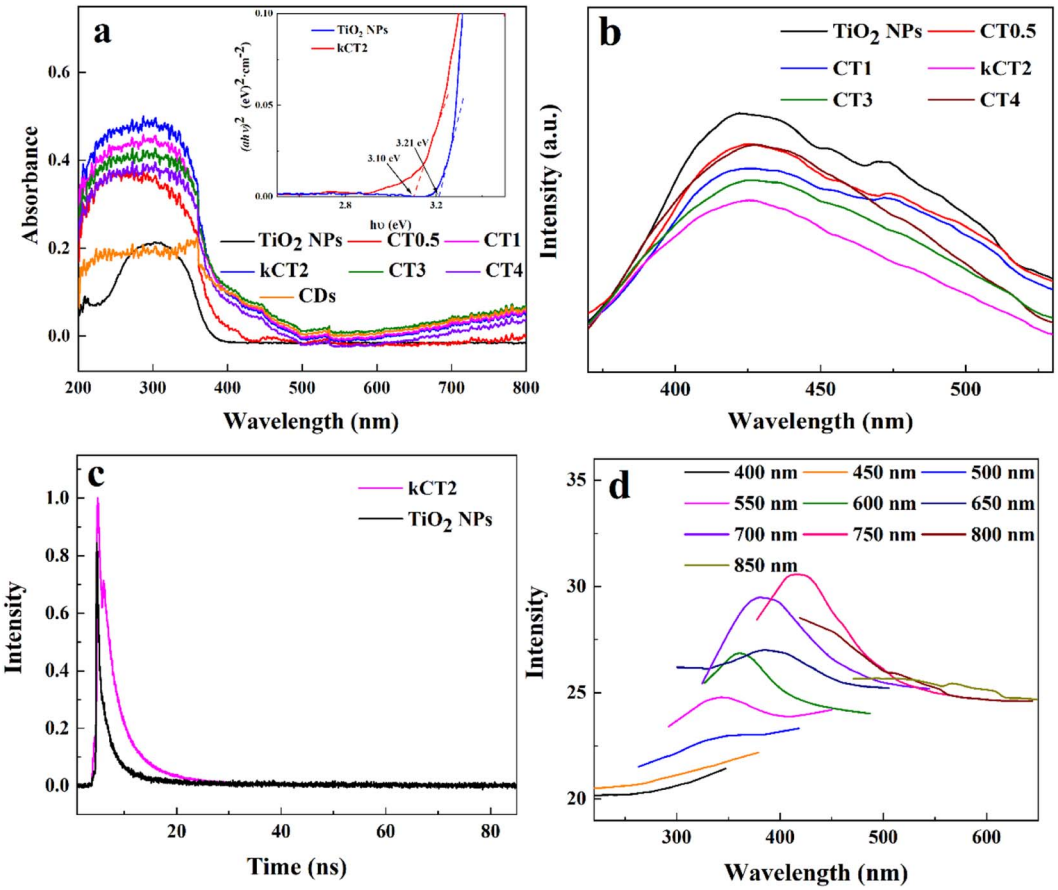

Fig. 7 UV-vis spectra of TiO_2 NPs and CDs/TiO_2 (a) and Tauc plots (inset) of TiO_2 NPs and kCT2, PL spectra of TiO_2 NPs and CDs/TiO_2 (b), TRPL spectra of TiO_2 NPs and kCT2 (c), and up-converted PL spectra of gCDs at different excitation wavelengths (d).

Table 2 TRPL data of TiO_2 NPs and kCT2

Sample	τ_1 (ns)	τ_2 (ns)	τ_{ave} (ns)
TiO_2 NPs	2.36	0.32	2.35
kCT2	3.03	3.04	3.03

wavelength less than 400 nm can be produced at the excitation wavelength of 400–700 nm. The emission light may be further applied to excite TiO_2 NPs to make more electrons jump to the conduction band (CB).[32]

Photoelectrochemical tests were carried out to investigate the separation and transmission of charges. In Fig. 8a the transient photocurrent responses of various photocatalysts are clearly observed by switching the light source for many cycles. Compared with TiO_2 NPs and gCDs, all the CDs/TiO_2 composites display improved photocurrent responses when irradiated with visible light. This indicates that more electrons move to the electrode substrate to gain a higher current and enable more efficient separation of charges under irradiation.[74] When the content of CDs increases, the photocurrent density rises first and then decreases, due to the fact that the excessive CDs could cover the reaction active sites and act as the recombination centers of charges.[75] So the kCT2 sample displays the strongest photocurrent signal, indicating high photocatalytic activity. The electrochemical impedance spectroscopy (EIS) plots of TiO_2 NPs, gCDs and kCT2 are used to study the transfer resistance and separation efficiency of charges with and without light irradiation (Fig. 8b). The arc radius of the samples is smaller under light than with no light, implying fast charge transfer under irradiation.[76] And the kCT2 sample has a smaller arc radius than TiO_2 NPs and gCDs in the Nyquist plot, suggesting its more efficient charge separation and transfer under irradiation similar to the PL and TRPL spectra. Furthermore, SPV experiments were carried out to understand the separation and transfer behavior of charges (Fig. 8c).[77,78] In general, a stronger SPV signal means a higher charge separation efficiency. It can be observed that the SPV response in the range of 350–400 nm denotes the electron transition from the VB to the CB of TiO_2 (band–band transition) under illumination.[79] Compared with TiO_2 NPs, the stronger SPV response for kCT2 means that more photo-excited electrons inject into the sample surface.[80] Therefore, the CDs/TiO_2 composite can significantly accelerate the charge separation, thereby enhancing the photocatalytic degradation of MO.

In order to ascertain the photo-degradation mechanism of MO over the CDs/TiO_2 composite, the reactive groups were

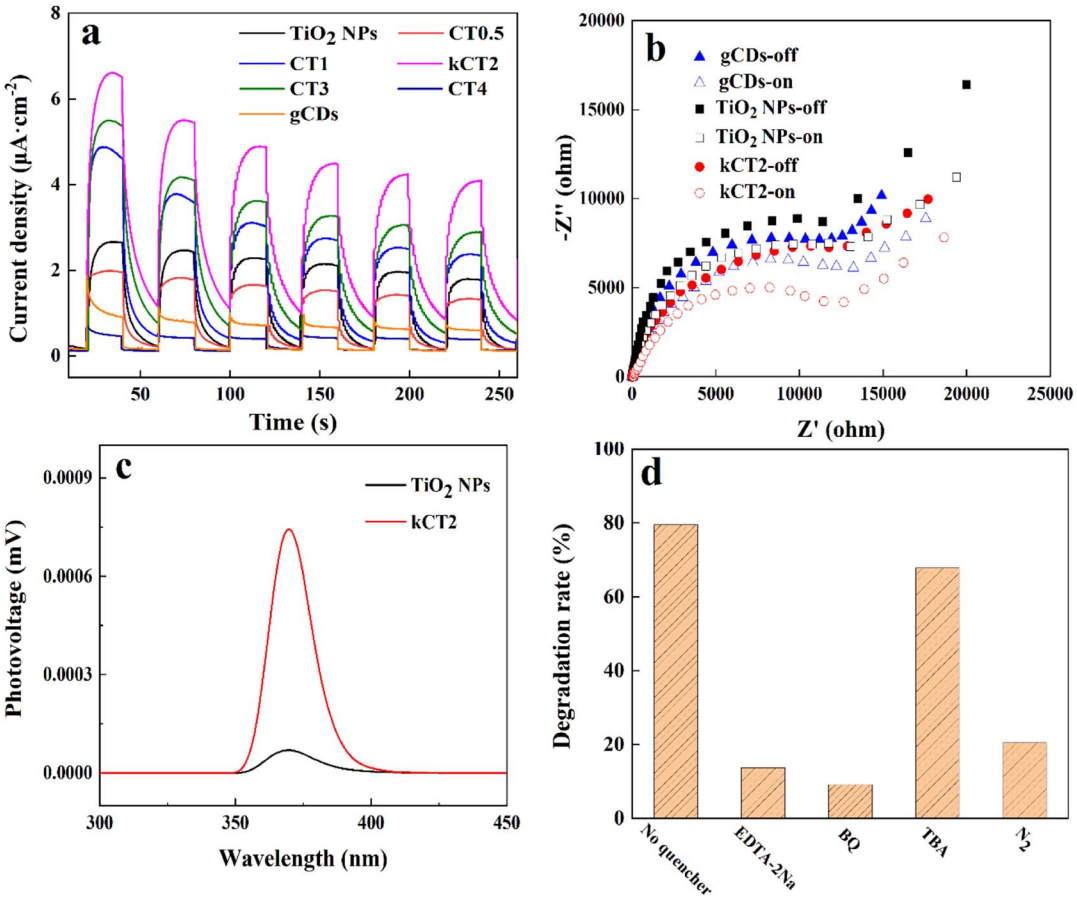

Fig. 8 Transient photocurrent responses of various samples (a), EIS plots of TiO_2 NPs, gCDs and kCT2 with and without light (b), SPV curves of TiO_2 NPs and kCT2 (c), and trapping experiments of active species for the MO removal over kCT2 under irradiation (d).

detected by trapping experiments (Fig. 8d). Generally speaking, the main active species such as ·OH, $\cdot O_2^-$ and h^+ are detected by TBA, BQ and EDTA-2Na, respectively.[81] It is found that the presence of BQ can severely prevent the degradation of MO and only 9.2% of MO is decomposed, and it is further proved by the N_2 experiment that the degradation of MO decreases rapidly due to the absence of O_2. Therefore, the $\cdot O_2^-$ is the main active group to participate in the photocatalytic reaction of MO. By using EDTA-2Na as a sacrificial agent, the MO degradation is also obviously prohibited with a MO removal of 13.8%. TBA also has an important influence on the MO removal and ·OH is involved in the photocatalytic reaction. So it is confirmed that $\cdot O_2^-$ and h^+ are the main active species and ·OH can also affect the photocatalytic degradation of MO.

As a model, NBT can be used to quantitatively analyze the $\cdot O_2^-$ species produced during the reaction, because $\cdot O_2^-$ can be captured by NBT.[36] The decrease of the absorption peak intensity of NBT at a maximum absorption of 259 nm with extension irradiation indicates that $\cdot O_2^-$ can be produced in the MO degradation (Fig. S7a†). The existence of ·OH in photocatalysis can be identified by reacting with TA using PL technology. The reaction product 2-TAOH of ·OH and TA has a characteristic fluorescence response at 425 nm.[36] The increasing PL intensity of 2-TAOH suggests that ·OH radicals are continuously produced in the photocatalytic reaction (Fig. S7b†). The above results are well matched to the trapping experiments.

In order to investigate the possible mechanism of photocatalytic degradation of MO over the kilogram-scale CDs/TiO_2 composite, it is necessary to clarify the VB and CB of TiO_2 NPs. According to the Mott–Schottky (M–S) curves (Fig. S8†), the positive slope indicates the n-type semiconductor feature of TiO_2 NPs.[82] The flat band potential (E_f) is −0.62 V (*vs.* Ag/AgCl) that can be converted to the reversible hydrogen electrode (RHE) using the formula $E_{RHE} = E^{\theta}_{(Ag/AgCl)} + 0.059 \times pH + E_{f(Ag/AgCl)}$, where $E^{\theta}_{(Ag/AgCl)}$ is 0.1976 V and the pH value is 7.[83–85] The E_f value of TiO_2 NPs is −0.0094 V (*vs.* RHE) and relative to the normal hydrogen electrode (NHE) is −0.42 V (*vs.* NHE). Based on the VB-XPS spectrum described in Fig. 4e, the VB of TiO_2 NPs is located at 2.21 V (*vs.* NHE). Using the formula $E_{CB} = E_{VB} - E_g$, the CB of TiO_2 NPs is calculated to be −1.0 V (*vs.* NHE).

A possible photocatalytic mechanism of MO degradation over the kilogram-scale CDs/TiO_2 composite is proposed in Fig. 9. The CDs/TiO_2 samples exhibit strong light absorption and enhanced photocatalytic activity towards MO, which is attributed to the introduction of CDs into TiO_2 NPs. Firstly, the electrons on CDs can be generated under irradiation due to the broad absorption band and transfer to the CB of TiO_2. The TiO_2 NPs modified with CDs can generate electrons by absorbing

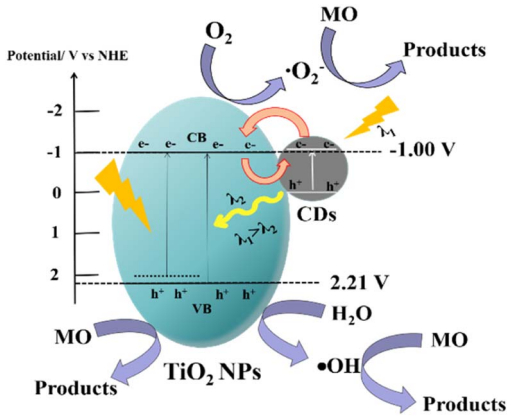

Fig. 9 Possible photo-degradation mechanism of MO over CDs/TiO_2.

visible light due to the narrowed band gap induced by the band tail states. The photo-generated electrons on the CB of TiO_2 can degrade MO molecules. Secondly, the short wavelength light that is emitted from the unique up-conversion of CDs can in turn be used to excite TiO_2 NPs to gain more photo-generated electrons and holes. Finally, the CDs as electron acceptors can receive the photo-induced electrons from TiO_2, which helps to block the charge recombination and makes more charge carriers available for MO degradation. At the same time, the adsorbed O_2 accumulated on the CB of TiO_2 and CDs is reduced to $\cdot O_2^-$ by reacting with photo-generated electrons to degrade MO. The h^+ on the VB of TiO_2 could directly decompose MO molecules. Moreover, due to the more positive VB, the partial h^+ can oxidize H_2O to generate $\cdot$OH radicals that can degrade MO. Therefore, the CDs/TiO_2 composite can gain the more photo-excited electrons and holes, and promote the transfer and separation of charges, so as to improve the photocatalytic activity.

4. Conclusions

Gram-scale CDs with a size of 2–5 nm were prepared, and the CDs/TiO_2 composites and the kilogram-scale CDs/TiO_2 material have been fabricated by one-step heat treatment. The CDs/TiO_2 composites exhibit superior photo-degradation performance towards MO, and the removal of MO increases from 12.4% for pure TiO_2 NPs to 88.8% for CT2 under visible light irradiation for 120 min. Moreover, kCT2 displays a similar photocatalytic activity towards MO to CT2 and the kilogram-scale synthesis of the CDs/TiO_2 composite has little effect on its morphology, crystallinity, surface features, chemical composition and photocatalytic performance. The excellent photocatalytic properties of the kilogram-scale CDs/TiO_2 composite may be due to the fact that the unique up-conversion of CDs, the existence of interaction at their interface and the narrowed band gap can broaden light absorption, excite the TiO_2 NPs to produce more electrons and holes, promote charge transfer and separation, and then degrade more MO molecules. This work proposes an economic and efficient strategy for the kilogram-scale synthesis of CDs/TiO_2, which exhibits their potential practical application in wastewater treatment.

Author contributions

JX, JZ and FT designed the experiments, analysed the data and wrote the article. PL and PZ collected the data.

Conflicts of interest

The authors declare no competing financial interest.

Acknowledgements

This work was supported by the National Natural Science Foundation of China (NSFC, Grant No. 51372154 and 20901051) and by the Zhejiang Provincial Natural Science Foundation of China under Grant No. LY21B010005. The authors thank Congxiang Ma from the Department of Chemistry and Chemical Engineering, Shaoxing University for help in the synthesis of the photocatalysts.

References

1 I. A. Mensah, M. Sun, A. Y. Omari-Sasu, C. Gao, E. S. Obobisa and T. T. Osinubi, *Environ. Sci. Pollut. Res.*, 2021, **28**, 56865–56891.
2 H. Wang, L. Fang, S. Hu, Y. Pei and W. Ma, *New J. Chem.*, 2018, **42**, 18335–18341.
3 C. Bathula, I. Rabani, S. Sekar, H.-K. Youi, J.-Y. Choy, A. Kadam, N. K. Shretha, Y.-S. Seo and H.-S. Kim, *Ceram. Int.*, 2021, **47**, 8732–8739.
4 R. P. Barkul, R. S. Sutar, M. K. Patil and S. D. Delekar, *ChemistrySelect*, 2021, **6**, 3360–3369.
5 K. Wang, L. Liang, Y. Zheng, H. Li, X. Niu, D. Zhang and H. Fan, *New J. Chem.*, 2021, **45**, 16168–16178.
6 D. V. Mousavi, S. Ahmadipouya, A. Shokrgozar, H. Molavi, M. Rezakazemi, F. Ahmadijokani and M. Arjmand, *J. Mol. Liq.*, 2021, **321**, 114487.
7 P. Ramesh, W. L. Xu, M. Sorci, C. Trant, S. Lee, J. Kilduff, M. Yu and G. Belfort, *J. Membr. Sci.*, 2021, **618**, 118699.
8 R. Kishor, D. Purchase, G. D. Saratale, L. F. Romanholo Ferreira, C. M. Hussain, S. I. Mulla and R. N. Bharagava, *J. Water Process. Eng.*, 2021, **43**, 102300.
9 M. Zhao, Y. Xiang, X. Jiao, B. Cao, S. Tang, Z. Zheng, X. Zhang, T. Jiao and D. Yuan, *Sep. Purif. Technol.*, 2021, **276**, 119289.
10 S. Hussain, H. Khan, N. Khan, S. Gul, F. Wahab, K. I. Khan, S. Zeb, S. Khan, A. Baddouh, S. Mehdi, A. F. Maldonado and M. Campos, *Environ. Technol. Innov.*, 2021, **22**, 101509.
11 Q. Wang, Y. Xiang, X. Li, W. Zhang, X. Huang and X. Qian, *Ind. Crops. Prod.*, 2021, **170**, 113695.
12 Y. Sun, L. Xu, P. Jin, X. Bai, X. Jin and X. Shi, *Chem. Eng. J.*, 2021, **405**, 126968.
13 M. Shams, H. Balouchi, H. Alidadi, F. Asadi, E. K. Goharshadi, S. Rezania, S. Rtimi, I. Anastopoulos,

Z. Bonyadi, K. Mehranzamir and D. A. Giannakoudakis, *J. Mol. Liq.*, 2021, **340**, 116917.
14 R. Guo, D. Zeng, Y. Xie, Y. Ling, D. Zhou, L. Jiang, W. Jiao, J. Zhao and S. Li, *Int. J. Hydrogen Energy*, 2020, **45**, 22534–22544.
15 X. Yang, Y. Wang, Z. Wang, X. Lv, H. Jia, J. Kong and M. Yu, *Ceram. Int.*, 2016, **42**, 7192–7202.
16 W. Kang, X. Jimeng and W. Xitao, *Appl. Surf. Sci.*, 2016, **360**, 270–275.
17 T. K. Jana, A. Pal, A. K. Mandal, S. Sarwar, P. Chakrabarti and K. Chatterjee, *ChemistrySelect*, 2017, **2**, 3068–3077.
18 X. Wang, H. Fan and P. Ren, *Catal. Commun.*, 2013, **31**, 37–41.
19 J. A. Mendoza, H. K. Kim, H. K. Park and K. Y. Park, *Korean J. Chem. Eng.*, 2012, **29**, 1483–1486.
20 M. Sun, X. Ma, X. Chen, Y. Sun, X. Cui and Y. Lin, *RSC Adv.*, 2014, **4**, 1120–1127.
21 X. T. Zhou, H. B. Ji and X. J. Huang, *Molecules*, 2012, **17**, 1149–1158.
22 F. Li, F. Tian, C. Liu, Z. Wang, Z. Du, R. Li and L. Zhang, *RSC Adv.*, 2015, **5**, 8389–8396.
23 S. Li, Y. Dong and M. Guo, *Appl. Surf. Sci.*, 2012, **258**, 8015–8018.
24 C. Liu, Y. Qin, W. Guo, Y. Shi, Z. Wang, Y. Yu and L. Wu, *Appl. Surf. Sci.*, 2022, **580**, 152262.
25 H. Feng, M.-H. Zhang and L. E. Yu, *Appl. Catal., A*, 2012, **413–414**, 238–244.
26 A. Qu, H. Xie, X. Xu, Y. Zhang, S. Wen and Y. Cui, *Appl. Surf. Sci.*, 2016, **375**, 230–241.
27 Z. Ma, H. Ming, H. Huang, Y. Liu and Z. Kang, *New J. Chem.*, 2012, **36**, 861–864.
28 W. Wang, L. Cheng and W. Liu, *Sci. China Chem.*, 2014, **57**, 522–539.
29 D. Bhattacharya, M. K. Mishra and G. De, *J. Phys. Chem. C*, 2017, **121**, 28106–28116.
30 E. Amadio, S. Cailotto, C. Campalani, L. Branzi, C. Raviola, D. Ravelli, E. Cattaruzza, E. Trave, A. Benedetti, M. Selva and A. Perosa, *Molecules*, 2019, **25**, 101.
31 B. Zhang, H. Maimaiti, D.-D. Zhang, B. Xu and M. Wei, *J. Photochem. Photobiol. A*, 2017, **345**, 54–62.
32 H. Zhang, H. Huang, H. Ming, H. Li, L. Zhang, Y. Liu and Z. Kang, *J. Mater. Chem.*, 2012, **22**, 10501–10506.
33 L.-Y. Lin, C. Liu and T.-T. Hsieh, *J. Catal.*, 2020, **391**, 298–311.
34 J. Zhao, Y. Li and P. Na, *Chin. J. Chem.*, 2021, **39**, 1310–1318.
35 A. Sekar and R. Yadav, *Optik*, 2021, **242**, 167311.
36 L. Ye, J. Liu, Z. Jiang, T. Peng and L. Zan, *Appl. Catal., B*, 2013, **142**, 1–7.
37 S. Sharma, A. Umar, S. K. Mehta, A. O. Ibhadon and S. K. Kansal, *New J. Chem.*, 2018, **42**, 7445–7456.
38 C. Xue, D. Li, Y. Li, N. Li, F. Zhang, Y. Wang, Q. Chang and S. Hu, *Ceram. Int.*, 2019, **45**, 17512–17520.
39 H. Zhang, G. Miao, X. Ma, B. Wang and H. Zheng, *Mater. Lett.*, 2014, **121**, 188–190.
40 G. Rajender, J. Kumar and P. K. Giri, *Appl. Catal., B*, 2018, **224**, 960–972.
41 J. Liu, W. Zhu, S. Yu and X. Yan, *Carbon*, 2014, **79**, 369–379.
42 H. Zhang, Z. Mo, H. Pei, Q. Jia, R. Wang, H. Feng, R. Guo and N. Liu, *J. Mater. Sci.: Mater. Electron.*, 2019, **31**, 1430–1441.
43 Y. Guo, X. Kong, Z. Liang, Y. Xue, H. Cui and J. Tian, *J. Colloid Interface Sci.*, 2020, **571**, 412–418.
44 D. Yan, Y. Liu, C.-y. Liu, Z.-y. Zhang and S.-d. Nie, *RSC Adv.*, 2016, **6**, 14306–14313.
45 S. Feizpoor and A. Habibi-Yangjeh, *Mater. Res. Bull.*, 2018, **99**, 93–102.
46 H. Niu, L. Liu, H. Wang, S. Zhang, Q. Ma, X. Mao, L. Wan, S. Miao and J. Xu, *Electrochim. Acta*, 2012, **81**, 246–253.
47 H. Zhang, X. Lv, Y. Li, Y. Wang and a. J. Li, *ACS Nano*, 2010, **4**, 380–386.
48 Z. Ai, L. Zhu, S. Lee and L. Zhang, *J. Hazard. Mater.*, 2011, **192**, 361–367.
49 Z. Liu, Z. Wang, S. Qing, N. Xue, S. Jia, L. Zhang, L. Li, N. Li, L. Shi and J. Chen, *Appl. Catal., B*, 2018, **232**, 86–92.
50 H. Bozetine, Q. Wang, A. Barras, M. Li, T. Hadjersi, S. Szunerits and R. Boukherroub, *J. Colloid Interface Sci.*, 2016, **465**, 286–294.
51 J. Zhang, S. Yan, S. Zhao, Q. Xu and C. Li, *Appl. Surf. Sci.*, 2013, **280**, 304–311.
52 X. Zhang, Y. Sun, X. Cui and Z. Jiang, *Int. J. Hydrogen Energy*, 2012, **37**, 811–815.
53 I. Amalraj Appavoo, J. Hu, Y. Huang, S. F. Li and S. L. Ong, *Water Res.*, 2014, **57**, 270–279.
54 J. Yu, Z. Chen, L. Zeng, Y. Ma, Z. Feng, Y. Wu, H. Lin, L. Zhao and Y. He, *Sol. Energy Mater. Sol. Cells*, 2018, **179**, 45–56.
55 J. Jia, D. Li, J. Wan and X. Yu, *J. Ind. Eng. Chem.*, 2016, **33**, 162–169.
56 M. Mukthar Ali, J. S. Arya Nair and K. Y. Sandhya, *Dyes Pigm.*, 2019, **163**, 274–284.
57 R. Purbia, R. Borah and S. Paria, *Inorg. Chem.*, 2017, **56**, 10107–10116.
58 Y. Zhang, Z. Zhao, J. Chen, L. Cheng, J. Chang, W. Sheng, C. Hu and S. Cao, *Appl. Catal., B*, 2015, **165**, 715–722.
59 R. Liu, H. Li, L. Duan, H. Shen, Y. Zhang and X. Zhao, *Ceram. Int.*, 2017, **43**, 8648–8654.
60 G. Li, F. Wang, P. Liu, Z. Chen, P. Lei, Z. Xu, Z. Li, Y. Ding, S. Zhang and M. Yang, *Chemosphere*, 2018, **197**, 526–534.
61 Y. Sui, L. Wu, S. Zhong and Q. Liu, *Appl. Surf. Sci.*, 2019, **480**, 810–816.
62 G. Jia, Y. Wang, X. Cui and W. Zheng, *ACS Sustain. Chem. Eng.*, 2018, **6**, 13480–13486.
63 J. Liu, L. Han, N. An, L. Xing, H. Ma, L. Cheng, J. Yang and Q. Zhang, *Appl. Catal., B*, 2017, **202**, 642–652.
64 H.-Y. Chen, L.-G. Qiu, J.-D. Xiao, S. Ye, X. Jiang and Y.-P. Yuan, *RSC Adv.*, 2014, **4**, 22491–22496.
65 W. Z. Tang and H. An, *Chemosphere*, 1995, 4157–4170.
66 J. Li, D. Luo, C. Yang, S. He, S. Chen, J. Lin, L. Zhu and X. Li, *J. Solid State Chem.*, 2013, **203**, 154–159.
67 J. Li, Z. Guo, Z. Liu, M. Cui and Z. Zhu, *Phys. Status Solidi A*, 2015, **212**, 459–466.
68 X. Li, P. Liu, Y. Mao, M. Xing and J. Zhang, *Appl. Catal., B*, 2015, **164**, 352–359.
69 S. Sharma, S. Kumar, S. M. Arumugam and S. Elumalai, *Appl. Catal., A*, 2020, **602**, 117730.

70 M. Sabri, A. Habibi-Yangjeh and S. Vadivel, *J. Mater. Sci.: Mater. Electron.*, 2019, **30**, 12510–12522.
71 M. A. Alcudia-Ramos, M. O. Fuentez-Torres, F. Ortiz-Chi, C. G. Espinosa-González, N. Hernández-Como, D. S. García-Zaleta, M. K. Kesarla, J. G. Torres-Torres, V. Collins-Martínez and S. Godavarthi, *Ceram. Int.*, 2020, **46**, 38–45.
72 M. S. Nasir, G. Yang, I. Ayub, X. Wang, S. Wang and W. Yan, *Int. J. Hydrogen Energy*, 2020, **45**, 13994–14005.
73 Y. Huang, Y. Wang, Y. Bi, J. Jin, M. F. Ehsan, M. Fu and T. He, *RSC Adv.*, 2015, **5**, 33254–33261.
74 P. Murugesan, S. Narayanan, M. Manickam, P. K. Murugesan and R. Subbiah, *Appl. Surf. Sci.*, 2018, **450**, 516–526.
75 D. Xu, L. Li, R. He, L. Qi, L. Zhang and B. Cheng, *Appl. Surf. Sci.*, 2018, **434**, 620–625.
76 W. Zhan, Y. Yuan, L. Sun, Y. Yuan, X. Han and Y. Zhao, *Small*, 2019, **15**, 1901024.
77 S. Li, L. Hou, L. Zhang, L. Chen, Y. Lin, D. Wang and T. Xie, *J. Mater. Chem. A*, 2015, **3**, 17820–17826.
78 J. Zhang, Y. Cao, P. Zhao, T. Xie, Y. Lin and Z. Mu, *Colloids Surf. A: Physicochem. Eng. Asp.*, 2020, **601**, 125019.
79 H. Li, D. Wang, H. Fan, P. Wang, T. Jiang and T. Xie, *J. Colloid Interface Sci.*, 2011, **354**, 175–180.
80 Y. Xin, Y. Lu, C. Han, L. Ge, P. Qiu, Y. Li and S. Fang, *Mater. Res. Bull.*, 2017, **87**, 123–129.
81 H. Yang, B. Xu, S. Yuan, Q. Zhang, M. Zhang and T. Ohno, *Appl. Catal., B*, 2019, **243**, 513–521.
82 J. Pan, Z. Dong, B. Wang, Z. Jiang, C. Zhao, J. Wang, C. Song, Y. Zheng and C. Li, *Appl. Catal., B*, 2019, **242**, 92–99.
83 R. A. Rather, M. Khan and I. M. C. Lo, *J. Catal.*, 2018, **366**, 28–36.
84 G. W. An, M. A. Mahadik, W.-S. Chae, H. G. Kim, M. Cho and J. S. Jang, *Appl. Surf. Sci.*, 2018, **440**, 688–699.
85 R. P. Patil, M. A. Mahadik, H.-S. Bae, W.-S. Chae, S. Hee Choi and J. Suk Jang, *Chem. Eng. J.*, 2020, **402**, 126153.